

Humidification of Central Asia and equatorward shifts of westerly winds since the late Pliocene

Yi Zhong¹, Xuefa Shi², Hu Yang^{3,4✉}, David J. Wilson⁵, James R. Hein⁶, Stefanie Kaboth-Bahr⁷, Zhengyao Lu⁸, Peter D. Clift⁹, Qing Yan¹⁰, Gerrit Lohmann³, Jiabo Liu^{1,11}, Francisco Javier González¹², Xiaodong Jiang¹, Zhaoxia Jiang¹³ & Qingsong Liu^{1,14,15✉}

The production, transport, and deposition of mineral dust exert major influences on climate change and Earth's biogeochemical cycles. Furthermore, their imprint, as recorded in pelagic sediments, provides an avenue for determining past changes in terrestrial aridity and atmospheric circulation patterns in response to global climate change. Here, by examining geochemical and magnetic data obtained from a ferromanganese crust in the western Pacific Ocean, we investigate the eolian dust source-region conditions and dust transport mechanisms from the Asian interior to the Pacific Ocean since the Pliocene. We identify a gradual provenance change in the dust source regions, from a dominant Gobi Desert source during the early Pliocene to a mixed Gobi-Taklimakan Desert source during the late Pliocene and Pleistocene, alongside increasing chemical weathering in those source areas. Climate model simulations suggest that these changes were related to an equatorward shift of the westerly jet and humidification of Central Asia during the gradual transition from a warm Pliocene climate to the cool Pleistocene.

¹Centre for Marine Magnetism (CM2) Department of Ocean Science and Engineering, Southern University of Science and Technology, 518055 Shenzhen, China. ²Key Laboratory of Marine Sedimentology and Metallogeny, First Institute of Oceanography, Ministry of Natural Resources (MNR), 266061 Qingdao, China. ³Alfred Wegener Institute, Helmholtz Centre for Polar and Marine Research, Bremerhaven, Germany. ⁴Southern Marine Science and Engineering Guangdong Laboratory, Zhuhai, China. ⁵Institute of Earth and Planetary Sciences, University College London and Birkbeck, University of London, London, UK. ⁶U.S. Geological Survey Retired, PCMSC, 2885 Mission Street, Santa Cruz, CA 95060, USA. ⁷Institute of Geosciences, University of Potsdam, Potsdam-Golm, Germany. ⁸Department of Physical Geography and Ecosystem Science, Lund University, Lund, Sweden. ⁹Department of Geology and Geophysics, Louisiana State University, Baton Rouge, LA, USA. ¹⁰Nansen-Zhu International Research Centre, Institute of Atmospheric Physics, Chinese Academy of Sciences, 100029 Beijing, China. ¹¹Paleomagnetism and Planetary Magnetism Laboratory, School of Geophysics and Geomatics, China University of Geosciences, 430074 Wuhan, China. ¹²Marine Geology Division, Geological Survey of Spain (IGME), 28003 Madrid, Spain. ¹³College of Marine Geosciences, Ocean University of China, 266100 Qingdao, China. ¹⁴Southern Marine Science and Engineering Guangdong Laboratory (Guangzhou), Guangzhou, China. ¹⁵Shanghai Sheshan National Geophysical Observatory, 201602 Shanghai, China. ✉email: hu.yang@awi.de; qslu@sustech.edu.cn

Since the late Oligocene, the Chinese Loess Plateau (CLP) sequences and the sediments of the North Pacific Ocean (NPO) have served as major sinks of Asian dust, preserving important evidence of past environmental changes in Central Asia^{1,2}. Conventionally, changes in wind strength and the moisture budget in Central Asian dust source regions have been regarded as the key factors controlling fluctuations in Asian eolian deposition over tectonic to millennial timescales³. Tectonic changes in the source regions (i.e., tectonically driven surface uplift) alongside shifts in atmospheric circulation patterns across the Asian continent (i.e., the westerly jet and the winter monsoon) have also been invoked as controlling processes in dust transport across Central Asia and into the adjacent Pacific Ocean^{4,5}. However, the lack of detailed terrestrial and marine records capturing changes in past dust transport between Central Asia and the Pacific Ocean hinders our understanding of the mechanisms driving dust fluxes in the past, and limits our insights into its potential evolution under impending global climate change.

Modern observations reveal that eolian dust plumes that reach the NPO are primarily controlled by the prevailing mid-latitude westerly winds, which predominantly carry particles from central and eastern Asian deserts^{6–8} (Fig. 1). As a result, past changes in the strength and/or position of the Northern Hemisphere mid-latitude winds could have influenced dust fluxes to the NPO, as proposed for the Pliocene⁹ and the late Pleistocene^{10,11}. Previous studies have also argued that eolian dust accumulation is closely linked to central Asian aridification, as well as to changes in the westerlies associated with Late Cenozoic cooling^{12,13}. However, the precise mechanisms responsible for increased dust accumulation rates across the CLP and the Pacific Ocean since the late Pliocene remain controversial. Instead of increased aridity in the source regions, the predominant driver could have been increased erosion, driven by enhanced monsoon precipitation or glaciation^{14,15}.

In this study, we reconstructed multi-proxy records from the late Miocene to recent in a slowly accreting hydrogenetic ferromanganese (Fe–Mn) crust from Site CM3D18 in the West Pacific Ocean (WPO) (Fig. 1 and Supplementary Fig. 1). We document a provenance change in the dust source regions alongside increased moisture-induced dust fluxes since the late Pliocene. Combined with existing records and new model simulations, we suggest that an equatorward shift of the westerlies and decreased evaporation in the source regions, resulting from global cooling, played important roles in controlling the dust flux from Central Asia to the Pacific Ocean.

Results

Eolian provenance change. Assuming a relatively constant flux of tephra from volcanic arc sources¹⁶, changes in the provenance of eolian dust could influence the Pb isotope composition of the eolian deposits in the WPO, as well as imprinting the seawater composition¹⁶. At present, deep water in this region originates as Lower Circumpolar Deep Water in the Southern Ocean¹⁷, and this situation was likely similar in the past. Although it has been proposed that enhanced deep-water ventilation occurred in the North Pacific during the late Miocene cooling¹⁸, the changes in Pb isotope composition in crust CM3D18 do not correspond to the timing of the proposed circulation changes (Supplementary Fig. 2). Hence, we suggest that the circulation changes did not extend to this region or did not exert an important control on the Fe–Mn crust Pb isotope record. In this case, variations in Pb isotope composition in the crust can be used to derive the relative contributions of eolian dust sources based on source mixing¹⁹. Such changes could be recorded in the composition of crust CM3D18 either directly due to changes in its siliciclastic detrital fraction, or indirectly via changes in the hydrogenetic Fe–Mn oxide framework signature acquired from local seawater¹⁶.

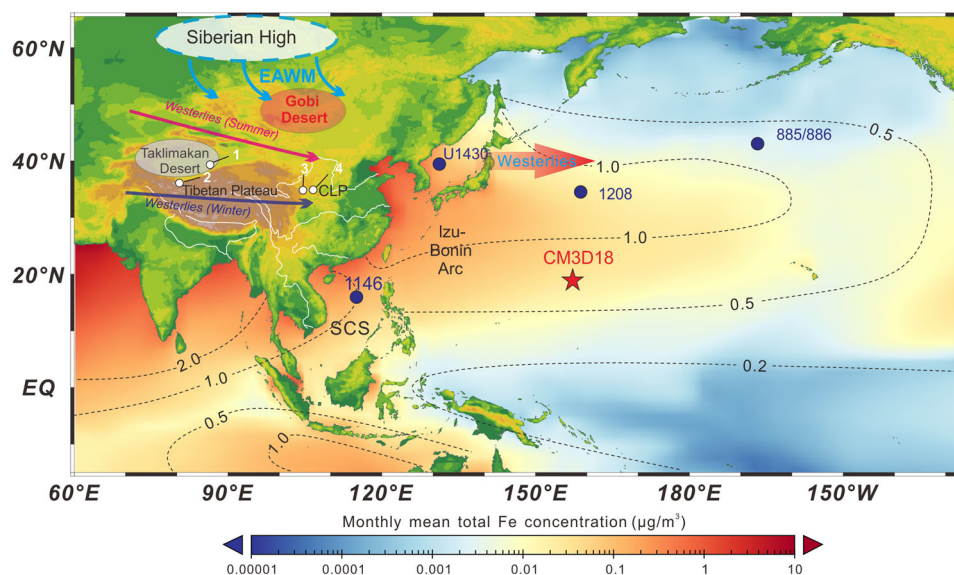


Fig. 1 Schematic atmospheric circulation and locations of key records (modified from Wan et al.⁶⁵). The major contribution of Asian dust to the North Pacific is indicated by monthly mean total iron concentrations ($\mu\text{g m}^{-3}$) based on Earth system modeling (color spectrum) and dust fluxes to the oceans ($\text{g cm}^{-2} \text{a}^{-1}$) (dotted lines)^{66,67}. Marine records include crust CM3D18 in the western Pacific Ocean (this study), IODP Site U1430 in the Sea of Japan²², ODP Site 1146 in the South China Sea (SCS)^{32,49}, and ODP Site 885/886^{13,23} and ODP Site 1208^{9,68} in the North Pacific. Terrestrial records include the sediment core from Lop Nor (No. 1)⁴⁰ and loess deposits (No. 2)¹² in the Tarim Basin of western China, and loess profiles from Baishui (No. 3)⁴⁶ and Lingtai (No. 4)⁴⁸ in the Chinese Loess Plateau (CLP). The shaded areas in the Asian interior are potential source regions of Asian dust in the Taklimakan Desert (China) and the Gobi Desert (Mongolia). Arrows indicate wind directions for the East Asian Winter Monsoon (EAWM; light blue) and the prevailing westerlies (dark blue arrow over land for winter; pink arrow over land for summer; thick red arrow over the ocean)⁶⁹. The locations of the July and January jet streams are from Ishizaka⁶.

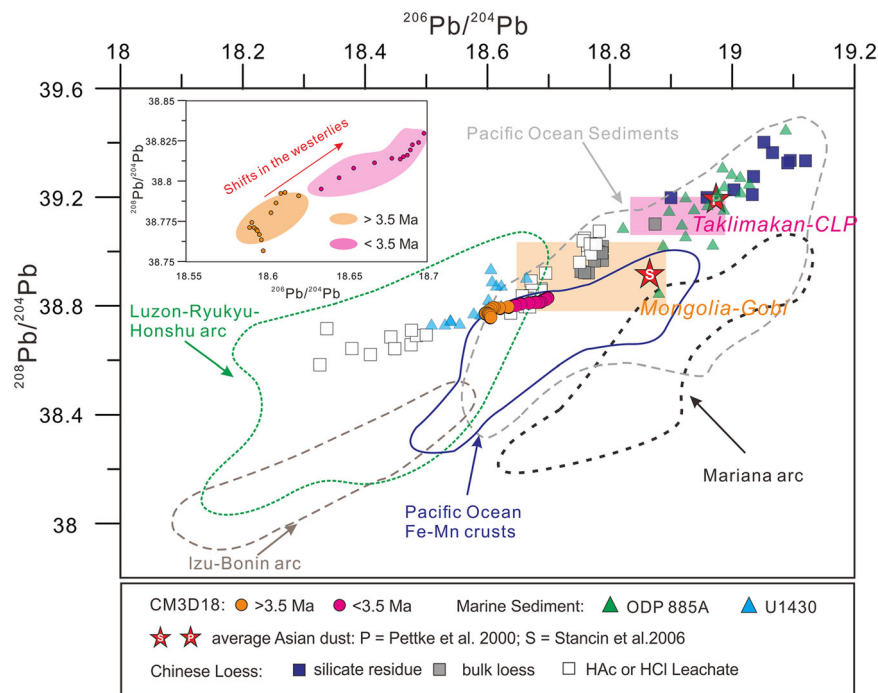


Fig. 2 Pb isotope data for Fe-Mn crust CM3D18 in comparison to other regional archives and input sources. Data sources: Pacific Ocean Fe-Mn crusts in the central NPO^{16,25–28}; Pacific Ocean detrital sediments^{20,23,70}; volcanic rocks of the Izu-Bonin arc, Mariana arc, and Luzon-Ryukyu-Honshu arc (compilations in Peate et al.³⁰); Chinese loess (bulk, residue, and leachates; refs. ^{16,20,71}); marine detrital downcore sediments from IODP Site U1430 in the Sea of Japan²² and ODP Site 885/886 in the North Pacific²³. Stars represent estimates for the average pre-anthropogenic composition of Asian dust^{23,72}, while typical compositions of the Chinese dust source areas are indicated for Mongolia-Gobi (orange-shaded box) and Taklimakan-CLP (pink-shaded box). Figure modified from Peate et al.³⁰. Inset panel is an expanded view of the Pb isotope variations in Fe-Mn crust CM3D18 separated according to age (orange, before 3.5 Ma; pink, since 3.5 Ma), with the red arrow indicating the general trend through time towards the present (see also Supplementary Fig. 4g), which is interpreted to reflect shifts in the westerly winds.

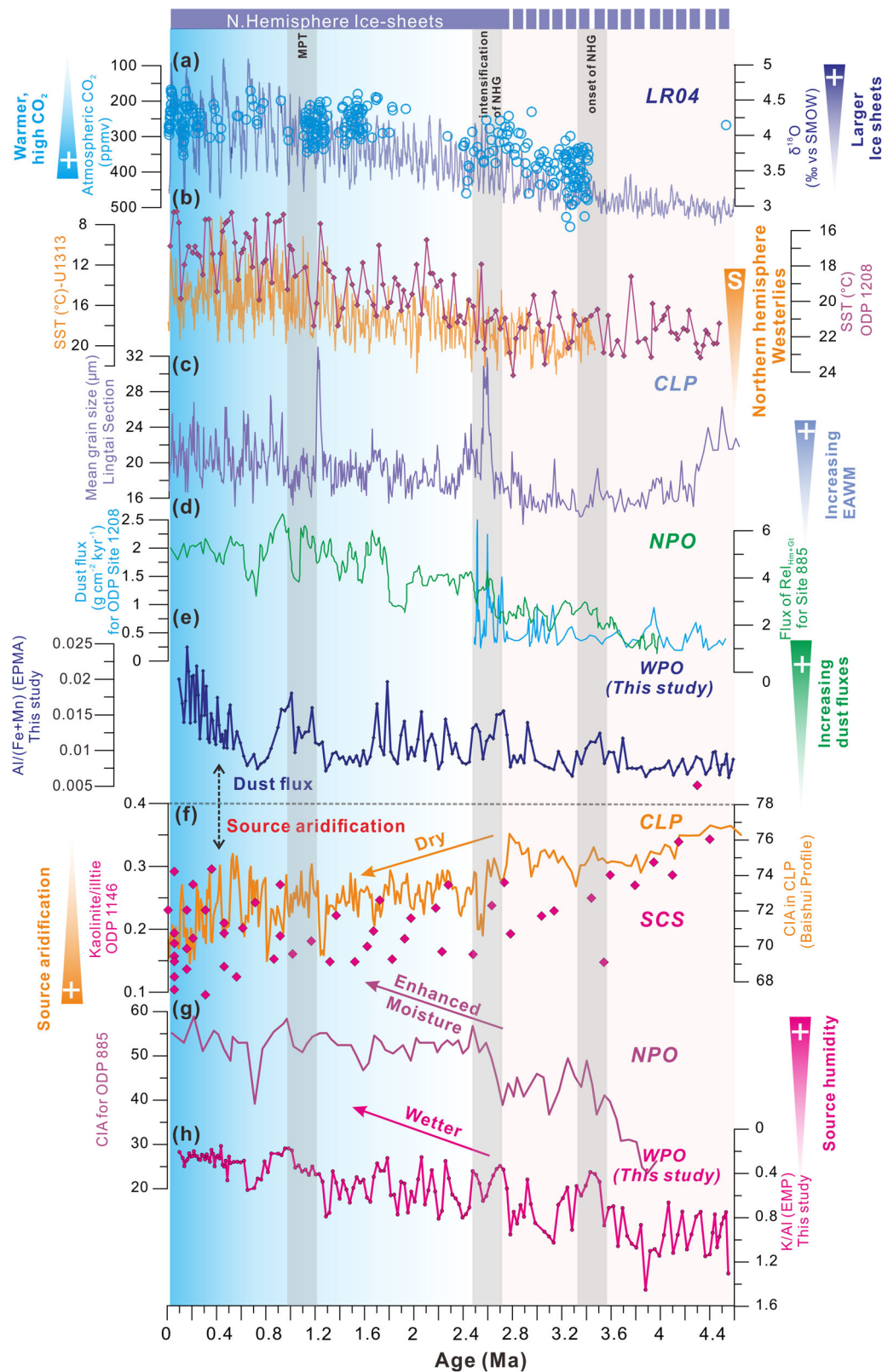
Previous studies have shown that the main sources of terrestrial sediment to the NPO are Chinese loess (dominant source in the Central Pacific Province)²⁰ and sediment from the young crustal provinces around the Pacific Rim (dominant source in the Marginal Province)²¹ (Supplementary Fig. 3). Detrital sediment data from International Ocean Discovery Program (IODP) Site U1430 within the Marginal Province of the NPO²² (Supplementary Fig. 3) have relatively unradiogenic lead (Pb) isotope compositions, partly reflecting those younger volcanic sources (Fig. 2). In contrast, the late Miocene to recent Pb isotope record from Ocean Drilling Program (ODP) Site 885 within the Central Province²³ (Supplementary Fig. 3) has a low tephra component and is relatively insensitive to arc-derived inputs because of the low concentrations of Pb in volcanic arc rocks (~5 ppm) compared to Chinese loess (~20 ppm; ref. ²⁴). Therefore, given the high eolian dust fluxes to this region⁷, the sediments from ODP Site 885 record a particularly radiogenic Pb isotope composition reflecting Asian dust sources (Fig. 2).

The Pb isotope composition of crust CM3D18 is compared to other Fe-Mn deposits in the central NPO and to potential regional Pb sources, such as arc volcanic rocks and Asian dust, as well as to existing dust records (Fig. 2). Crust CM3D18 has higher $^{208}\text{Pb}/^{204}\text{Pb}$ and lower $^{206}\text{Pb}/^{204}\text{Pb}$ ratios than most Pacific Ocean Fe-Mn deposits^{16,25–28} (Fig. 2), as also seen in Fe-Mn crusts from the Izu-Bonin basin^{29,30}. Proximal volcanic inputs from the Izu-Bonin and Mariana arcs were evidently insignificant contributors to the Pb in Pacific Ocean Fe-Mn crusts and crust CM3D18 (Fig. 2), because arc volcanic rocks have significantly lower $^{208}\text{Pb}/^{204}\text{Pb}$ values, and lower $^{208}\text{Pb}/^{204}\text{Pb}$ values for a given $^{206}\text{Pb}/^{204}\text{Pb}$ value³⁰. Instead, crust CM3D18 has Pb isotope compositions that overlap with the isotopic range of leachable Pb in Chinese loess^{16,20}, which differs from the Pb

isotope composition of the silicate fraction of those dust particles (Fig. 2), suggesting a dominant Chinese loess source. Experiments on Chinese loess revealed the presence of an easily leachable component adsorbed onto the surface of grains that has a different Pb isotope composition to that of the silicate dust particles^{16,20}. The leachable adsorbed component on the loess grains was originally derived from the condensation of atmospheric volcanic aerosols¹⁶. Importantly, distinct differences are also observed between the Pb isotope composition of Chinese loess from the Mongolia-Gobi Desert and the Taklimakan-CLP sources (Fig. 2).

Subsamples of crust CM3D18 older than 3.5 Ma have relatively unradiogenic Pb isotope compositions that are similar in composition to the Mongolia-Gobi dust source^{16,31}, although with a possible mixing trend towards the less radiogenic Pb isotope compositions of arc volcanic rocks from provinces such as Luzon-Ryukyu or Honshu (Fig. 2). Detrital sediment data from IODP Site U1430 within the Marginal Province of the NPO²² also plot on an array that fans out from a Chinese loess end-member towards the volcanic arc fields (Fig. 2), suggesting a similar set of Pb sources in both settings. Subsamples of crust CM3D18 younger than 3.5 Ma have more radiogenic Pb isotope compositions (Fig. 2), with a trend towards the more radiogenic composition of Taklimakan-CLP dust sources, suggesting an increasing contribution from this source through time (Fig. 2).

Synchronous changes of dust flux and source moisture. To enable a comparison of changes in dust flux and source moisture, we compare elemental ratio proxies from crust CM3D18 with existing literature data in Fig. 3. Since Al is resistant to leaching while K is more mobile during chemical weathering, the $\text{K}_2\text{O}/\text{Al}_2\text{O}_3$ ratio in detrital sediments is commonly used to trace the



degree of chemical weathering^{32,33}. The siliciclastic Ca input is low in remote deep-sea settings and the Ca content is mostly a function of biogenic carbonate content (in water depths shallower than the carbonate compensation depth). Hence, the Fe/Ca ratio can potentially be used to estimate the siliciclastic flux relative to biogenic carbonate productivity. Meanwhile, the Al/(Fe+Mn) ratios, which are determined by Al content, provide an effective

indicator of terrigenous dust input, as supported by co-variations between Al and other indicators of clay input, such as K, Cs, and Rb concentrations.

We observe strong co-variation between chemical weathering proxies (K/Al) (Fig. 3h) and eolian indicators (Al/(Fe+Mn) ratio) (Fig. 3e) from the Pacific Ocean in the Pliocene, which suggests that high dust accumulation rates were linked to more humid

Fig. 3 Land-ocean comparison among records from the Chinese Loess Plateau (CLP), South China Sea (SCS), North Pacific Ocean (NPO), and West Pacific Ocean (WPO). **a** Atmospheric CO₂ (ppm)⁵⁷ and global benthic LR04 $\delta^{18}\text{O}$ stack⁷³; **b** Northern Hemisphere sea surface temperature (SST) reconstructions from IODP Site U1313 in the North Atlantic⁷⁴ and ODP Site 1208 in the North Pacific⁷⁵; **c** Mean grain size of eolian deposits in the CLP Lingtai profile⁴⁸; **d** Flux of Rel_{Him+Gt} at ODP Site 885 as an indicator of dust inputs¹⁵ and dust flux at ODP Site 1208⁹; **e** Al/(Fe+Mn) (count ratio) in crust CM3D18 (this study); **f** Kaolinite/illite at ODP Site 1146 from the South China Sea³², and chemical index of alteration (CIA) in the CLP Baishui profile⁴⁶; **g** CIA at ODP Site 885¹⁵; **h** K/Al (count ratio) in crust CM3D18 (this study). Blue bars at the top of the figure indicate the development of the Northern Hemisphere ice sheets⁷⁶. Gray vertical bars indicate the onset and intensification of Northern Hemisphere Glaciation (NHG) and the Mid-Pleistocene Transition (MPT).

conditions in some of the dust source areas (Fig. 3 and Supplementary Fig. 4). Both Al/(Fe+Mn) (Supplementary Fig. 4c) and Fe/Ca ratios in crust CM3D18 (Supplementary Fig. 4b) are proxies for eolian input to the WPO and appear to have increased at ~3.5 Ma, ~2.7 Ma, and ~1.2 Ma (gray bars in Fig. 3; dashed lines in Supplementary Fig. 4). Hence, there appears to be a link between dust flux and the onset and enhancement of Northern Hemisphere Glaciation (NHG), which was also associated with a decline in atmospheric carbon dioxide levels (Fig. 3a). The inferred eolian dust changes in crust CM3D18 at ~3.5 Ma (Supplementary Fig. 4b and c) match well with eolian dust flux reconstructions from IODP Site U1430 in the Sea of Japan²² (Supplementary Fig. 4h) and ODP Site 885/886 in the NPO¹³ (Supplementary Fig. 4i), whereas the changes at ~2.7 Ma and ~1.2 Ma are better resolved in the NPO records (Supplementary Fig. 4i) than in the Sea of Japan²² (Supplementary Fig. 4h).

In addition, the hard isothermal remanent magnetization (HIRM) parameter (Supplementary Fig. 4e) and remanence coercivity (B_{cr}) (Supplementary Fig. 4f) provide a measure of the relative concentration of high-coercivity magnetic minerals (hematite) in the sediment, which has been used as an eolian proxy in the northern Sahara region³⁴ and at ODP Site 885 in the NPO³¹. Consistent with those studies, the hematite content in crust CM3D18 (Supplementary Fig. 4e, f) was also elevated during the Pleistocene when a high dust supply from Central Asia is inferred from the other geochemical records. Detailed rock magnetic results (Supplementary Fig. 5) also support an increase in detrital magnetic mineral contents after 3.5 Ma.

Modeling results. Since the late Miocene, Earth's climate has primarily been characterized by global cooling associated with decreasing atmospheric greenhouse gas concentrations (Fig. 3a). To examine the potential environmental factors contributing to the changes in Western Pacific dust flux, we conducted two climate simulations with different atmospheric CO₂ forcing ($p\text{CO}_2$; i.e., 284 and 568 ppmv) using the Alfred Wegener Institute-Earth System Model (AWI-ESM) for the coupled atmosphere-ocean-sea ice-vegetation system (see “Methods”). The higher $p\text{CO}_2$ experiment is used to mimic the climate for the relatively warm late Miocene and Pliocene, while the lower $p\text{CO}_2$ experiment serves as a reference simulation for the Pleistocene. Other boundary conditions, such as the land-sea distribution, orbital configuration, and continental ice-sheet distribution were fixed to the pre-industrial conditions, and hence their effects were not explored.

The Northern Hemisphere westerly winds reach their southernmost position and strongest intensity during the boreal winter^{4,5}, contributing significantly to the dust transportation from Central Asia to the Pacific Ocean. Since the dust can also be transported during the autumn and spring, when there is less snow coverage, we analyzed the wind changes between October and March in our model simulations (Fig. 4). For a cooling climate, a systematic equatorward shift of the Northern Hemisphere westerly winds is detected, with anomalous westerly winds at 20°–40°N and anomalous easterly winds from 40°–60°N (Fig. 4b). These changes would contribute to a shift in the dust

source region from the Mongolia-Gobi Desert to the Taklimakan-CLP (Fig. 2 and Supplementary Fig. 4g). Such a shift in the westerly winds is attributed to strengthened and equatorward shifted mid-latitude meridional temperature gradients, associated with global cooling^{9,35}.

We further evaluate the aridity changes in the global cooling experiments, revealing a shrinking of the arid zone over Central Asia (Fig. 5). This change is primarily induced by a decrease in the potential evaporation as a result of surface cooling (Supplementary Fig. 6b). In addition, an equatorward shift of the westerly winds³⁵ also brings more precipitation to Central Asia (Supplementary Fig. 6a). In combination, our dust proxy records and model simulations provide consistent evidence for a trend towards less arid conditions in Central Asia as a result of global cooling since the late Miocene.

Discussion

Currently, the WPO primarily receives dust from central and eastern Asian deserts via the prevailing westerly winds between ~25°N and 45°N (Fig. 1), and this dust has a distinctive Pb isotopic composition that is related to its source regions²⁰. Detrital sediments in the low- to mid-latitudes (25–35°N) of the NPO have a radiogenic ²⁰⁸Pb/²⁰⁴Pb signature (>39.3), whereas these values gradually decrease towards higher latitudes (>40°N) (Supplementary Fig. 3). These latitudinal variations in Pb isotope signatures run subparallel to the distributions of the Taklimakan-CLP (²⁰⁸Pb/²⁰⁴Pb ~ 39.1–39.2) and Mongolia-Gobi (²⁰⁸Pb/²⁰⁴Pb ~ 38.8–38.9) dust sources in Central Asia (Fig. 2). This observation suggests that transport pathways for tropospheric dust are strongly linked to latitude³⁶, while there is also an influence on detrital sediment signatures from the surrounding volcanic provinces^{20,21}.

The provenance transition recorded by Pb isotopes in crust CM3D18 during the Pliocene (Fig. 2 and Supplementary Fig. 4g) broadly matches with increases in eolian dust fluxes recorded in this crust (Fig. 3e and Supplementary Fig. 4b, c, e–f). These changes also coincide with dust flux changes at ODP Site 885/886¹³ from the North Pacific (Supplementary Fig. 4i) and IODP Site U1430²² from the Sea of Japan (Supplementary Fig. 4h), overall indicating rapid increases in eolian deposition at ~3.5 Ma and ~2.7 Ma. In the context of Plio-Pleistocene long-term cooling, the late Pliocene (~3.5 Ma) was marked by an increase in global benthic stable oxygen isotope ($\delta^{18}\text{O}$) values and lower $p\text{CO}_2$, indicating the onset of NHG (Fig. 3a). Moreover, deep-sea records of ice-rafted debris indicate significant circum-Arctic glaciations starting around ~3.6 Ma³⁷, with synchronous development of ice sheets in Greenland, Scandinavia, and North America at ~2.7–2.6 Ma³⁸ (Fig. 3a). Theoretically, a colder climate should be accompanied by stronger equator-to-pole temperature gradients and equatorward shifts of the westerlies, as revealed by Northern Hemisphere paleo-temperature reconstructions³⁹ (Fig. 3b). Such changes in the temperature gradient would have strengthened the Siberian High, leading to a southward shift in the Northern Hemisphere westerlies (Fig. 4) and accompanying changes in dust sources to the WPO (Fig. 2). Therefore, whereas the initial response of dust input to environmental changes in the Tarim Basin⁴⁰ may have been a transient

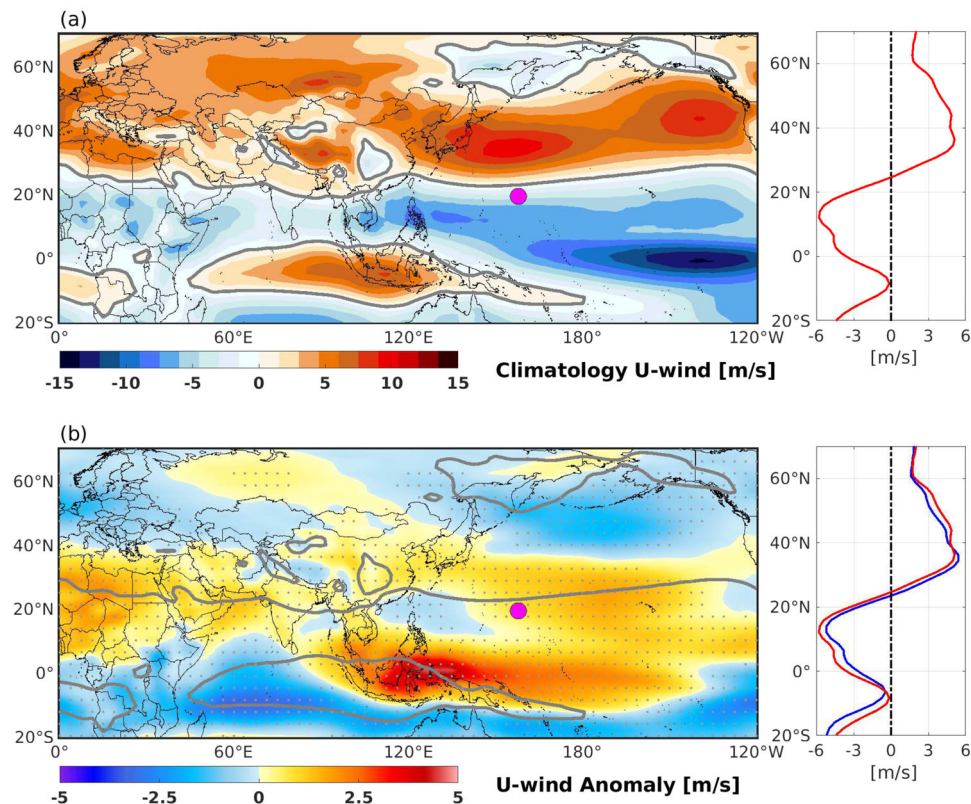


Fig. 4 Climatology and anomaly of zonal wind at 850 hPa pressure level during October to March. **a** Climatology zonal wind (u-component) based on the last 100 years of the AWI-ESM 568 ppmv CO₂ experiment. Positive values represent westerly wind, and negative values represent easterly wind. The right panel shows the mean zonal wind in this experiment. **b** Zonal wind anomaly in the AWI-ESM 284 ppmv experiment with respect to the 568 ppmv CO₂ experiment (i.e., Exp284-Exp568). The right panel shows the mean zonal wind in the Exp284 (blue line) and Exp568 (red line) experiments. An equatorward shift of the westerly jet can be identified in the low-CO₂ experiment. Gray contours represent zero-crossing of the climatology zonal wind from easterly to westerly. The gray stippling indicates areas where the anomalies are statistically significant (two tailed Student's *t*-test). The pink circle indicates the location of crust CM3D18.

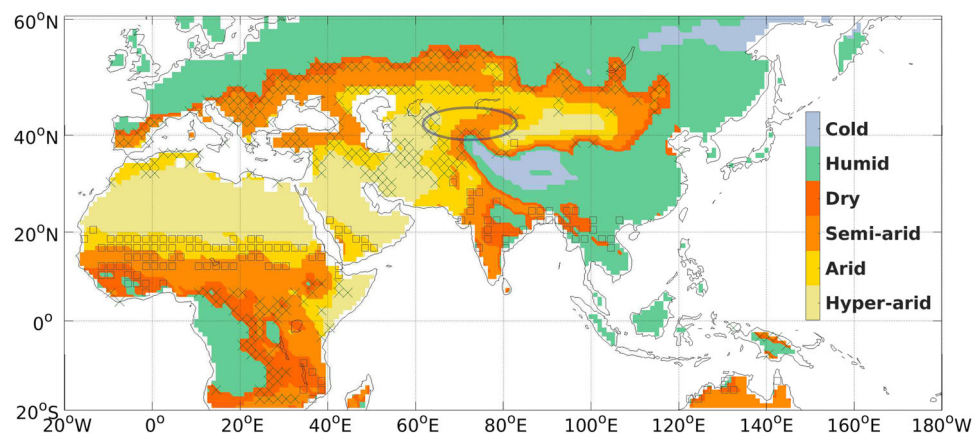


Fig. 5 Change in the aridity pattern in the AWI-ESM low-CO₂ experiment compared to the high-CO₂ experiment. Colors indicate aridity according to the Aridity Index (AI) based on the high-CO₂ experiment (i.e., AWI-ESM simulation with CO₂ at 568 ppmv). The AI is defined as the ratio between annual mean precipitation and potential evaporation: Hyper-arid (AI < 0.05), Arid (0.05 < AI < 0.2), Semi-arid (0.2 < AI < 0.5), Dry (0.5 < AI < 0.65), Humid (AI > 0.65), Cold (yearly potential evaporation < 400 mm). The blue crosses mark regions where the climate type changed to more humid conditions in the low-CO₂ experiment compared to the high-CO₂ experiment. The black squares mark regions where the climate type changed towards more arid conditions in the low-CO₂ experiment. These dry and wet transition regions are identified based on the AI index. Overall, less arid conditions are observed over Central Asia in the low-CO₂ experiment. The blue oval indicates the approximate location of the Tarim Basin.

effect, the southward shift of the Northern Hemisphere westerlies could have helped to maintain a persistent (if relatively minor) input from the Taklimakan Desert to the WPO during the Pliocene-Pleistocene^{9,41}.

Although the Taklimakan Desert gradually became a significant Asian interior dust source during the late Miocene and early Pliocene⁴² (Fig. 2), there are many stages associated with particle formation, mobilization, transport, deposition, re-mobilization, and

re-deposition that may have been involved⁴³. The formation of dust deposits requires a source of dust, adequate wind energy to entrain and transport the dust to the terrestrial deposition site, and conditions that favor trapping and preservation of the dust at that site^{3,44,45}. The co-variation among chemical weathering proxies (Fig. 3g, h) and eolian records (Fig. 3d, e) in the Pacific Ocean during the late Pliocene and Pleistocene indicates that high dust accumulation rates were linked to more humid conditions in the dust source areas (Fig. 5). This observation emphasizes that dust is only likely to have been generated from restricted areas within the Asian interior where renewable fine-grained sediment sources were available^{15,43}, and indicates that high dust fluxes at ~2.7 Ma and ~1.2 Ma were likely controlled by hydrological weathering associated with the enhancement of NHG. Based on our climate modeling experiment, we find that humidification over Central Asia was primarily due to a decrease in potential evaporation (Fig. 5 and Supplementary Fig. 6).

Interestingly, the weathering changes inferred for the source regions have divergent temporal patterns in records from the CLP⁴⁶ and South China Sea^{32,47} (Fig. 3f) when compared to records from the Pacific Ocean¹⁵ (Fig. 3g, h). Hence, a land-ocean comparison of dust fluxes and weathering changes between the CLP and the Pacific Ocean during the late Pliocene and Pleistocene provides further insight into the different processes influencing the formation and transport of Asian dust (Fig. 3). Specifically, the coupled trends in dust records between the CLP and the South China Sea since the intensification of NHG (Fig. 3c, d) likely reflect increased eolian inputs controlled mainly by stronger northwesterly winter-spring monsoon surface winds in the CLP region^{43,48,49}. In contrast, the accompanying reduction in evaporation at high elevations around the Tarim Basin would have led to wetter conditions that enhanced weathering (Fig. 3g, h), and produced a significant amount of fine-grained material⁵⁰ of a grain size that could be entrained in wind for longer, enabling it to travel thousands of kilometers when lifted up into the jet stream (Supplementary Fig. 7), and thereby influence the more distal records (Fig. 3d, e).

In summary, proximal dust flux and grain size changes in the CLP largely responded to the enhanced transport strength related to Plio-Pleistocene global cooling and glaciation, and those sediments were characterized by a lower chemical weathering intensity, whereas the more distal Pacific Ocean records were more strongly influenced by the availability of fine-grained and more weathered terrestrial dust sources. Our provenance and dust proxy records, in combination with climate modeling experiments, suggest that the humidification of Central Asia and equatorward shifts of the westerly winds were the dominant controls on the enhanced dust flux to the WPO since the late Pliocene. Furthermore, $p\text{CO}_2$ decreases, global cooling, and ice-sheet expansion may have provided the primary forcing for these changes.

Methods

Sampling and age model. The Fe-Mn crust CM3D18 was dredged from CM Guyot in the Marcus-Wake Seamount Group (19.4344°N, 157.987°E, mean water depth 2480 m) (Fig. 1) by the R/V *Dayang Yihao*. The crust is 53 mm thick, with a flat surface and subparallel dark brown layering (Supplementary Fig. 1a). It was accreted on a basaltic hyaloclastite substrate. Secondary features such as carbonate fluorapatite phosphatization were not observed (Supplementary Fig. 1c). The outer 30 mm was studied here and can be categorized into two layers: the older Layer 1 is 16 mm thick and shows columnar texture, while the younger Layer 2 is 14 mm thick and shows dendritic-mottled and columnar texture (Supplementary Fig. 1c). The transition between the layers is gradational over 30 mm, rather than abrupt.

The subsamples display a continuous decline in $^{10}\text{Be}/^9\text{Be}$ ratios with increasing depth in the crust from 0 to 30 mm (Supplementary Table 1). Average growth rates and ages were calculated based on linear interpolation between those data points (Supplementary Fig. 1b), with growth rates between 2.7 and 7.9 mm/Ma being similar to the typical range of 1–5 mm/Ma for central Pacific crusts⁵¹. High-

resolution electron probe micro-analyzer (EPMA) chemistry, bulk chemical composition, rock magnetic data, and Pb isotope compositions were analyzed from subsamples of the crust; for analytical results, see Supplementary Figs. 8 and 9 and Supplementary Table 2. The elemental data indicate a hydrogenetic origin for the crust (Supplementary Fig. 10).

Major element measurements. The Fe-Mn crust was cut vertically at 2 mm intervals and a total of 14 subsamples were scraped from top to bottom for geochemical analyses and magnetic measurements. Major element concentrations were determined using a Thermo-Fisher IRIS II Intrepid XSP inductively coupled plasma optical emission spectrometer (ICP-OES). Additional trace elements, including rare earth elements and yttrium (REY), were analyzed by inductively coupled plasma mass spectrometry (ICP-MS) using a Perkin-Elmer ELAN 9000 ICP-MS at the Institute of Oceanology, Chinese Academy of Sciences (IOCAS) in Qingdao, China. The dissolution procedure was as follows: 0.05 g of sample powder was digested in a sealed Teflon beaker with 0.5 ml HF, 0.5 ml HNO_3 , and 1.5 ml HCl on a hot plate (120 °C) for ~12 h. Following heating to dryness, 1 ml HNO_3 and 1 ml H_2O were added, and the beaker was sealed and heated on a hot plate (150 °C) for ~12 h to dissolve the residue. The major and trace elements were analyzed using internal calibrations with reference materials (GBW07315, GBW07316, BCR-2, BHVO-2, GBW07295, GBW07296, NOD-P-1, NOD-A-1).

Polished thin sections were analyzed by EPMA using a JEOL JXA-8230 Electron Probe WDS/EDS Micro Analyzer (JEOL, Tokyo, Japan) at the State Key Laboratory of Marine Geology, Tongji University. The analyses were performed with a beam of ~2 µm diameter, using an accelerating voltage of 15 kV, and a beam current of 10 nA. In total, 524 points were analyzed at an average interval of 0.1 mm along a vertical transect through the crust perpendicular to the growth layers.

Mineral magnetic measurements. The subsamples were dried in an oven at a temperature below 40 °C and then placed in $2 \times 2 \times 2 \text{ cm}^3$ plastic cubes to conduct magnetic measurements. Low- and high-frequency mass-specific magnetic susceptibility (χ_{lf} and χ_{hf}) were measured using a multifunction Kappabridge (MFK-FA) with frequencies of 976 Hz and 15,616 Hz, respectively. An alternating field (AF) was applied to each sample using a D-2000 AF demagnetizer, with a peak field of 100 mT and a direct current (DC) bias field of 0.05 mT, to obtain the anhysteretic remanent magnetization (ARM), which is regarded as representative of the stable single-domain (SD) ferrimagnetic content⁵². The susceptibility of anhysteretic remanent magnetization (χ_{ARM}) was obtained by dividing the ARM by the DC bias (0.05 mT). Saturation isothermal remanent magnetization (SIRM) was imparted to the z-axis for each sample in a DC field of 1.0 T using an IM-10-30 Impulse Magnetizer and the SIRM value was measured using the JR-6A Spinner Magnetometer (AGICO). The values of SIRM depend primarily on the magnetic mineral content, and secondarily on the magnetic crystal grain size, while superparamagnetic domains are irrelevant. A saturation isothermal remanent magnetization was imparted in a 1.0 T applied field, termed $\text{SIRM}_{1.0 \text{ T}}$. Subsequently, samples were demagnetized with backfields of -100 and -300 mT, and the corresponding remanence was measured, termed $\text{IRM}_{-100 \text{ mT}}$ and $\text{IRM}_{-300 \text{ mT}}$. The parameter $\text{HIRM}_{300 \text{ mT}}$ is defined as $0.5 \times (\text{SIRM}_{1.0 \text{ T}} + \text{IRM}_{-300 \text{ mT}})$, and the S-ratio is defined as $\text{IRM}_{-300 \text{ mT}}/\text{SIRM}_{1.0 \text{ T}}$ ⁵³. Hysteresis loops and first order reversal curves (FORCs) were measured up to maximum applied fields of 1.0 T for samples using a vibrating sample magnetometer (VSM, LakeShore 8600). The saturation magnetization (M_s) and coercivity (B_c) were obtained after high-field slope correction. The remanence coercivity (B_{cr}) was obtained by direct current demagnetization of $\text{SIRM}_{1.0 \text{ T}}$ back to -1.0 T. For every sample, a total of 100 FORCs were measured with a maximum field of 400 mT and an averaging time of 500 ms. The FORC diagrams were processed using the software "FORCinel"⁵⁴ with a constant smoothing factor of five. Principle component analysis (FORC-PCA) was also performed using "FORCinel" following the protocols of Lascu et al.⁵⁵. Magnetic measurements were performed at the Centre for Marine Magnetism (CM²), Southern University of Science and Technology in China.

Pb isotope measurements. Lead (Pb) isotopic compositions were measured on Fe-Mn crust samples following digestion using a mixture of ultrapure HF and HNO_3 and purification using conventional ion-exchange chromatography. Isotopic analysis was performed using a Nu Instruments multi-collector ICP-MS housed at the State Key Laboratory of Isotope Geochemistry, Guangzhou Institute of Geochemistry, Chinese Academy of Sciences. Internal analytical uncertainty was estimated based on repeated measurements of the Pb reference material NIST 981, using Tl-doping for mass bias correction⁵⁶, indicating an internal reproducibility for Pb isotope ratios of better than 200 ppm/amu. Repeated analyses of the USGS W-2a standard gave a reproducibility of $^{206}\text{Pb}/^{204}\text{Pb} = 16.946 \pm 0.001$, $^{207}\text{Pb}/^{204}\text{Pb} = 15.506 \pm 0.001$, $^{208}\text{Pb}/^{204}\text{Pb} = 36.745 \pm 0.001$ (2sd, $n = 30$).

Climate simulations. The global climate since the late Miocene has primarily been characterized by gradual cooling attributed to a decrease in atmospheric greenhouse gas concentrations⁵⁷. We conducted a CO_2 experiment using the AWI Earth System Model (AWI-ESM, ref. 58) to understand the forcing mechanism for the dust flux and provenance changes. Two simulations were performed forced by different $p\text{CO}_2$ concentrations of 284 and 568 ppmv, respectively. The former value

represents a relatively cold climate, which is used to mimic the Pleistocene, while the latter value represents a relatively warm climate state, which mimics the late Miocene and Pliocene climate. Both simulations were integrated for 500 years, and the last 100 years of the model results were used. The AWI-ESM has previously been validated^{59,60} and widely applied to investigate the present climate state and paleoclimate changes^{41,61–64}.

Data availability

High-resolution electron probe micro-analyzer (EPMA) chemistry, bulk chemical composition, rock magnetic data and Pb isotope data are included in <https://doi.org/10.5281/zenodo.7238351>.

Code availability

The AWI-ESM code is publicly available at <https://fesom.de/models/awi-esm/>.

Received: 16 May 2022; Accepted: 26 October 2022;

Published online: 10 November 2022

References

- Guo, Z. T. et al. Onset of Asian desertification by 22 Myr ago inferred from loess deposits in China. *Nature* **416**, 159–163 (2002).
- Pettke, T., Halliday, A. N. & Rea, D. K. Cenozoic evolution of Asian climate and sources of Pacific seawater Pb and Nd derived from eolian dust of sediment core LL44-GPC3. *Paleoceanography* **17**, PA000673 (2002).
- Sun, Y. et al. Source-to-sink fluctuations of Asian eolian deposits since the late Oligocene. *Earth Sci. Rev.* **200**, 102963 (2020).
- Yan, Y., Ma, L. & Sun, Y. B. Tectonic and climatic controls on provenance changes of fine-grained dust from the Chinese Loess Plateau since the late Oligocene. *Geochim. Cosmochim. Acta* **200**, 110–122 (2017).
- Zhang, Q., Liu, Q. S., Li, J. H. & Sun, Y. B. An integrated study of the eolian dust in pelagic sediments from the North Pacific Ocean based on environmental magnetism, transmission electron microscopy and diffuse reflectance spectroscopy. *J. Geophys. Res. Solid Earth* **122**, 3358–3376 (2018).
- Ishizaka, T. In *Kosa: Atmosphere and Hydrosphere Sciences* (ed. N. U. Research Center for Atmosphere Hydrosphere) 109–123 (Kokin Shoin, 1994).
- Rea, D. K. The paleoclimatic record provided by eolian deposition in the deep sea: The geologic history of wind. *Rev. Geophys.* **32**, 159–195 (1994).
- Uno, I. et al. Asian dust transported one full circuit around the globe. *Nat. Geosci.* **2**, 557–560 (2009).
- Abell, J. T., Winckler, G., Anderson, R. F. & Herbert, T. D. Poleward and weakened westerlies during Pliocene warmth. *Nature* **589**, 70–75 (2021).
- Gray, W. R. et al. Wind-driven evolution of the North Pacific subpolar gyre over the last deglaciation. *Geophys. Res. Lett.* **47**, e2019GL086328 (2020).
- Lora, J. M., Mitchell, J. L., Risi, C. & Tripathi, A. E. North Pacific atmospheric rivers and their influence on western North America at the Last Glacial Maximum. *Geophys. Res. Lett.* **44**, 1051–1059 (2017).
- Fang, X. M. et al. The 3.6-Ma aridity and westerlies history over midlatitude Asia linked with global climatic cooling. *Proc. Natl Acad. Sci. USA* **117**, 24729–24734 (2020).
- Rea, D. K., Snoeckx, H. & Joseph, L. H. Late Cenozoic eolian deposition in the North Pacific: Asian drying, Tibetan uplift, and cooling of the northern hemisphere. *Paleoceanography* **13**, 215–224 (1998).
- Nie, J. S., Pullen, A., Garzione, C. N., Peng, W. B. & Wang, Z. Pre-Quaternary decoupling between Asian aridification and high dust accumulation rates. *Sci. Adv.* **4**, eaao6977 (2018).
- Zhang, Q. et al. Mechanism for enhanced eolian dust flux recorded in North Pacific Ocean sediments since 4.0 Ma: aridity or humidity at dust source areas in the Asian interior? *Geology* **48**, 77–81 (2020).
- Ling, H. F. et al. Differing controls over the Cenozoic Pb and Nd isotope evolution of deepwater in the central North Pacific Ocean. *Earth Planet. Sci. Lett.* **232**, 345–361 (2005).
- Kawabe, M. & Fujio, S. Pacific ocean circulation based on observation. *J. Oceanogr.* **66**, 389–403 (2010).
- Zhai, L. et al. Deep-water formation in the North Pacific during the late Miocene global cooling. *Paleoceanogr. Paleoclimatol.* **36**, e2020PA003946 (2021).
- Erhardt, A. M. et al. Assessing sedimentary detrital Pb isotopes as a dust tracer in the Pacific Ocean. *Paleoceanogr. Paleoclimatol.* **4**, e2020PA004144 (2021).
- Jones, C. E., Halliday, A. N., Rea, D. K. & Owen, R. M. Eolian inputs of lead to the North Pacific. *Geochim. Cosmochim. Acta* **64**, 1405–1416 (2000).
- Nakai, S., Halliday, A. N. & Rea, D. K. Provenance of dust in the Pacific Ocean. *Earth Planet. Sci. Lett.* **119**, 143–157 (1993).
- Shen, X. et al. History of Asian eolian input to the Sea of Japan since 15 Ma: Links to Tibetan uplift or global cooling? *Earth Planet. Sci. Lett.* **474**, 296–308 (2017).
- Pettke, T., Halliday, A. N., Hall, C. M. & Rea, D. K. Dust production and deposition in Asia and the north Pacific Ocean over the past 12 Myr. *Earth Planet. Sci. Lett.* **178**, 397–413 (2000).
- Gallet, S., Jahn, B. M. & Torii, M. Geochemical characterization of the Luochuan loess-paleosol sequence, China, and paleoclimatic implications. *Chem. Geol.* **133**, 67–88 (1996).
- Abouchami, W., Goldstein, S. L., Galer, S. J. G., Eisenhauer, A. & Mangini, A. Secular changes of lead and neodymium in central Pacific seawater recorded by a Fe-Mn crust. *Geochim. Cosmochim. Acta* **61**, 3957–3974 (1997).
- Christensen, J. N. Climate and ocean dynamics and the lead isotopic records in Pacific ferromanganese crusts. *Science* **277**, 913–918 (1997).
- Ling, H. F. et al. Evolution of Nd and Pb isotopes in Central Pacific seawater from ferromanganese crusts. *Earth Planet. Sci. Lett.* **146**, 1–12 (1997).
- van de Fliedert, T. et al. Lead isotopes in North Pacific deep water—implications for past changes in input sources and circulation patterns. *Earth Planet. Sci. Lett.* **209**, 149–164 (2003).
- Chu, N. C. et al. Evidence for hydrothermal venting in Fe isotope compositions of the deep Pacific Ocean through time. *Earth Planet. Sci. Lett.* **245**, 202–217 (2006).
- Peate, D. W., Falkner, L. & Ken, A. J. R. Pb isotope variations in hydrogenetic Fe–Mn crusts from the Izu–Bonin fore-arc. *Chem. Geol.* **258**, 288–298 (2009).
- Bailey, I. et al. Iron fertilisation and biogeochemical cycles in the sub-Arctic northwest Pacific during the late Pliocene intensification of northern hemisphere glaciation. *Earth Planet. Sci. Lett.* **307**, 253–265 (2011).
- Clift, P. D., Wan, S. M. & Blusztajn, J. Reconstructing chemical weathering, physical erosion and monsoon intensity since 25 Ma in the northern South China Sea: a review of competing proxies. *Earth Sci. Rev.* **130**, 86–102 (2014).
- Lupker, M., France-Lanord, C., Galy, V., Lave, J. & Kudrass, H. Increasing chemical weathering in the Himalayan system since the Last Glacial Maximum. *Earth Planet. Sci. Lett.* **365**, 243–252 (2013).
- Larrasoana, J. C., Roberts, A. P., Rohling, E. J., Winkhofer, M. & Wehausen, R. Three million years of monsoon variability over the northern Sahara. *Clim. Dyn.* **21**, 689–698 (2003).
- Yang, H. et al. Tropical expansion driven by poleward advancing midlatitude meridional temperature gradients. *J. Geophys. Res. Atmos.* **125**, e2020JD033158 (2020).
- Zhao, W. et al. Hf–Nd isotopic variability in mineral dust from Chinese and Mongolian deserts: implications for sources and dispersal. *Sci. Rep.* **4**, 5837 (2014).
- Haug, G. H., Sigman, D. M., Tiedemann, R., Pedersen, T. F. & Sarnthein, M. Onset of permanent stratification in the subarctic Pacific Ocean. *Nature* **401**, 779–782 (1999).
- Kleiven, H. F., Jansen, E., Fronval, T. & Smith, T. M. Intensification of Northern Hemisphere glaciations in the circum Atlantic region (3.5–2.4 Ma)–ice-rafted detritus evidence. *Palaeogeogr. Palaeoclimatol. Palaeoecol.* **184**, 213–223 (2002).
- De Schepper, S., Gibbard, P. L., Salzmann, U. & Ehlers, J. A global synthesis of the marine and terrestrial evidence for glaciation during the Pliocene Epoch. *Earth Sci. Rev.* **135**, 83–102 (2014).
- Liu, W. G. et al. Late Miocene episodic lakes in the arid Tarim Basin, Western China. *Proc. Natl Acad. Sci. USA* **111**, 16292–16296 (2014).
- Yang, H. et al. Poleward shift of the major ocean gyres detected in a warming climate. *Geophys. Res. Lett.* **47**, e2019GL085868 (2020).
- Sun, J. M., Zhang, Z. Q. & Zhang, L. Y. New evidence on the age of the Taklimakan Desert. *Geology* **37**, 159–162 (2009).
- Pye, K. & Zhou, L. P. Late Pleistocene and Holocene aeolian dust deposition in North China and the Northwest Pacific Ocean. *Palaeogeogr. Palaeoclimatol. Palaeoecol.* **73**, 11–23 (1989).
- Meijer, N. et al. Identifying eolian dust in the geological record. *Earth Sci. Rev.* **211**, 103410 (2020).
- Tsoar, H. & Pye, K. Dust transport and the question of desert loess formation. *Sedimentology* **34**, 139–153 (1987).
- Xiong, S. F., Ding, Z. L., Zhu, Y. J., Zhou, R. & Lu, H. J. A ~6 Ma chemical weathering history, the grain size dependence of chemical weathering intensity, and its implications for provenance change of the Chinese loess–red clay deposit. *Quater. Sci. Rev.* **29**, 1911–1922 (2010).
- Wan, S., Li, A., Clift, P. D. & Stuu, J. B. W. Development of the East Asian monsoon: Mineralogical and sedimentologic records in the northern South China Sea since 20 Ma. *Palaeogeogr. Palaeoclimatol. Palaeoecol.* **254**, 561–582 (2007).
- Sun, Y., An, Z., Clemens, S. C., Bloemendal, J. & Vandenberghe, J. Seven million years of wind and precipitation variability on the Chinese Loess Plateau. *Earth Planet. Sci. Lett.* **297**, 525–535 (2010).

49. Wan, S., Li, A., Stuut, J. B. W. & Xu, F. Grain-size records at ODP site 1146 from the northern South China Sea: implications on the East Asian monsoon evolution since 20 Ma. *Sci. China Ser. D Earth Sci.* **50**, 1536–1547 (2007).
50. Sun, J. M. Source regions and formation of the loess sediments on the high mountain regions of Northwestern China. *Quat. Res.* **58**, 341–351 (2002).
51. Hein, J. R. et al. In *Handbook of Marine Mineral Deposits*, (ed. Cronan, D. S.) 239–279 (CRC Press, 2000).
52. Oldfield, F. Environmental magnetism—a personal perspective. *Quat. Sci. Rev.* **10**, 73–85 (1991).
53. King, J. W. & Channell, J. E. T. Sedimentary magnetism, environmental magnetism, and magnetostratigraphy. *Rev. Geophys.* **29**, 358–370 (1991).
54. Harrison, R. J. & Feinberg, J. M. FORC_{in}: an improved algorithm for calculating first-order reversal curve distributions using locally weighted regression smoothing. *Geochem. Geophys. Geosyst.* **9**, Q05016 (2008).
55. Lasca, I. et al. Magnetic unmixing of first-order reversal curve diagrams using principal component analysis. *Geochem. Geophys. Geosyst.* **16**, 2900–2915 (2015).
56. Collerson, K. D., Kamber, B. S. & Schoenberg, R. Applications of accurate, high-precision Pb isotope ratio measurement by multi-collector ICP-MS. *Chem. Geol.* **188**, 65–83 (2002).
57. Rae, J. W. B. et al. Atmospheric CO₂ over the Past 66 Million Years from Marine Archives. *Ann. Rev. Earth Planet. Sci.* **49**, 609–641 (2021).
58. Sidorenko, D. et al. Evaluation of FESOM2.0 coupled to ECHAM6.3: Preindustrial and HighResMIP simulations. *J. Adv. Model. Earth Syst.* **11**, 3794–3815 (2019).
59. Sidorenko, D. et al. Towards multi-resolution global climate modeling with ECHAM6-FESOM. Part I: model formulation and mean climate. *Clim. Dyn.* **44**, 757–780 (2015).
60. Brierley, C. M. et al. Large-scale features and evaluation of the PMIP4-CMIP6 mid-Holocene simulations. *Clim. Past* **16**, 1847–1872 (2020).
61. Brown, J. R. et al. Comparison of past and future simulations of ENSO in CMIP5/PMIP3 and CMIP6/PMIP4 models. *Clim. Past* **16**, 1777–1805 (2020).
62. Lohmann, G. et al. Abrupt climate and weather changes across timescales. *Paleoceanogr. Paleoclimatol.* **35**, e2019PA003782 (2020).
63. Shi, X. & Lohmann, G. Simulated response of the mid-Holocene Atlantic meridional overturning circulation in ECHAM6-FESOM/MPIOM. *J. Geophys. Res. Oceans* **121**, 6444–6469 (2016).
64. Shi, X., Lohmann, G., Sidorenko, D. & Yang, H. Early-Holocene simulations using different forcings and resolutions in AWI-ESM. *Holocene* **30**, 996–1015 (2020).
65. Wan, S., Sun, Y. B. & Nagashima, K. Asian dust from land to sea: processes, history and effect from modern observation to geological records. *Geol. Magaz.* **157**, 701–706 (2020).
66. Hamilton, D. S. et al. Improved methodologies for Earth system modelling of atmospheric soluble iron and observation comparisons using the Mechanism of Intermediate complexity for Modelling Iron (MIMI v1.0). *Geosci. Model Dev.* **12**, 3835–3862 (2019).
67. Jickells, T. D. et al. Global iron connections between dust, ocean biogeochemistry and climate. *Science* **308**, 67–71 (2005).
68. LaRiviere, J. P. et al. Late Miocene decoupling of oceanic warmth and atmospheric carbon dioxide forcing. *Nature* **486**, 97–100 (2012).
69. Merrill, J. T., Uematsu, M. & Bleck, R. Meteorological analysis of long range transport of mineral aerosols over the North Pacific. *J. Geophys. Res. Atmos.* **94**, 8584–8598 (1989).
70. Godfrey, L. V. Temporal changes in the lead isotopic composition of red clays: comparison with ferromanganese crust records. *Chem. Geol.* **185**, 241–254 (2002).
71. Biscaye, P. E. et al. Asian provenance of glacial dust (stage 2) in the Greenland Ice Sheet Project 2 Ice Core, Summit, Greenland. *J. Geophys. Res. Oceans* **102**, 26765–26781 (1997).
72. Stancin, A. M. et al. Radiogenic isotopic mapping of late Cenozoic eolian and hemipelagic sediment distribution in the east-central Pacific. *Earth Planet. Sci. Lett.* **248**, 840–850 (2006).
73. Lisiecki, L. E. & Raymo, M. E. A Pliocene-Pleistocene stack of 57 globally distributed benthic $\delta^{18}\text{O}$ records. *Paleoceanography* **20**, PA1003 (2005).
74. Naafs, B. D. A., Voelker, A. H. L., Karas, C., Andersen, N. & Sierro, F. J. Repeated near-collapse of the Pliocene sea surface temperature gradient in the North Atlantic. *Paleoceanogr. Paleoclimatol.* **35**, e2020PA003905 (2020).
75. Herbert, T. D. et al. Late Miocene global cooling and the rise of modern ecosystems. *Nat. Geosci.* **9**, 843–847 (2016).
76. Westerhold, T. An astronomically dated record of Earth's climate and its predictability over the last 66 million years. *Science* **369**, 1383–1387 (2020).

Acknowledgements

We thank Junsheng Nie, Shiming Wan, Hong Ao, and Niels Meijer for helpful suggestions, and the China Ocean Sample Repository for supplying samples. We also thank Dr. Joe Aslin and three anonymous reviewers for their insightful input, which helped us to improve the final manuscript. This work was supported financially by the National Natural Science Foundation of China (grants 42274094, 92158208, 41874078, 42176245, 42104068, and 42274096), the State Key Laboratory of Marine Geology, Tongji University (No. MGK202209), the opening foundation (SSKP202101) of the Shanghai Sheshan National Geophysical Observatory (Shanghai, China), the State Key Laboratory of Marine Geology, Shenzhen Science and Technology Program (KQTD20170810111725321), and the China Postdoctoral Science Foundation (2020M682770). DJW is supported by a NERC independent research fellowship (NE/T011440/1). S.K.-B. acknowledges an Open-Topic Post-Doc Fellowship from the University of Potsdam and received funding from the German Academic Exchange Service (DAAD; grant numbers 57558354 and 57603159). We acknowledge support by the Open Access Publication Funds of Alfred-Wegener-Institut Helmholtz-Zentrum für Polar- und Meeresforschung.

Author contributions

Y.Z. and Q.S.L. conceived the study. X.F.S. collected the sample. H.Y., Z.Y.L., and Q.Y. performed simulation analysis. D.J.W., J.R.H., S.K.-B., P.D.C., and F.J.G. contributed to interpretation and discussion. G.L. contributed to modeling design and discussion. X.D.J., J.B.L., and Z.X.J. contributed to proxy analysis. Y.Z. led the manuscript writing with intellectual contributions from all authors.

Funding

Open Access funding enabled and organized by Projekt DEAL.

Competing interests

The authors declare no competing interests.

Additional information

Supplementary information The online version contains supplementary material available at <https://doi.org/10.1038/s43247-022-00604-5>.

Correspondence and requests for materials should be addressed to Hu Yang or Qingsong Liu.

Peer review information *Communications Earth & Environment* thanks Yonggang Liu and the other, anonymous, reviewer(s) for their contribution to the peer review of this work. Primary handling editors: Kerstin Schepanski and Joe Aslin, Aliénor Lavergne. Peer reviewer reports are available.

Reprints and permission information is available at <http://www.nature.com/reprints>

Publisher's note Springer Nature remains neutral with regard to jurisdictional claims in published maps and institutional affiliations.



Open Access This article is licensed under a Creative Commons Attribution 4.0 International License, which permits use, sharing, adaptation, distribution and reproduction in any medium or format, as long as you give appropriate credit to the original author(s) and the source, provide a link to the Creative Commons license, and indicate if changes were made. The images or other third party material in this article are included in the article's Creative Commons license, unless indicated otherwise in a credit line to the material. If material is not included in the article's Creative Commons license and your intended use is not permitted by statutory regulation or exceeds the permitted use, you will need to obtain permission directly from the copyright holder. To view a copy of this license, visit <http://creativecommons.org/licenses/by/4.0/>.

© The Author(s) 2022